batteries

MDPI

Article

Improvement of Cycling Stability of Core–Shell Structured Ni-Rich NMC Cathodes by Using a Tungsten Oxide Stabilization Interlayer

Bilal Tasdemir *, Svitlana Krüger, Pinank Sohagiya, Apurba Ray and Bilge Saruhan *

German Aerospace Center (DLR e.V), Institute for Frontier Materials on Earth and in Space, Linder Hoehe, 51147 Cologne, Germany; svitlana.krueger@dlr.de (S.K.); pinank.sohagiya@dlr.de (P.S.); apurba.ray@dlr.de (A.R.)
* Correspondence: bilal.tasdemir@dlr.de (B.T.); bilge.saruhan@dlr.de (B.S.)

Abstract

The growing demand for higher-energy lithium-ion batteries, encompassing consumer electronics, stationary grid storage, and electric mobility to specialized sectors like aerospace, medical devices, and industrial robotics, requires cathode materials that offer higher capacity while remaining cost-effective. This trend has intensified the development of nickel-rich $LiNi_{1-x-y}Mn_xCo_yO_2$ (NMC) systems. However, high-Ni NMCs such as $LiNi_{0.9}Mn_{0.05}Co_{0.05}O_2$ (NMC90) suffer from limited thermal and cycling stability. Core–shell architectures using $LiNi_{0.6}Mn_{0.2}Co_{0.2}O_2$ (NMC622) as a shell can partially alleviate these drawbacks, but structural degradation caused by interdiffusion between the core and shell persists as a major challenge. This study investigates whether a tungsten oxide interlayer can act as a protective barrier that suppresses interdiffusion, stabilizes the crystal structure, and improves long-term electrochemical performance. In this work, NMC cathode powders were synthesized via a one-pot oxalate co-precipitation route, followed by structural characterization using X-ray diffraction (XRD), scanning electron microscopy (SEM), X-ray photoelectron spectroscopy (XPS), and ion scattering spectroscopy (ISS). Electrochemical performance, including capacity retention, cycling stability, and internal resistance, was evaluated through galvanostatic charge–discharge (GCD) testing and electrochemical impedance spectroscopy (EIS). The core–shell configuration delivered higher specific discharge capacity compared to the individually synthesized core-only and shell-only reference materials, and the incorporation of a tungsten oxide interlayer resulted in a twofold increase in cycle life. These results demonstrate that tungsten oxide effectively enhances cycling stability by inhibiting core–shell interdiffusion, offering a promising pathway toward more durable high-Ni NMC cathodes.

Keywords: Ni-rich NMC; tungsten oxide; core–shell; coating; co-precipitation; oxalic acid; cyclic stability

Academic Editor: Yong-Joon Park

Received: 28 January 2026
Revised: 19 February 2026
Accepted: 23 February 2026
Published: 27 February 2026

1. Introduction

The transition toward a carbon-neutral global economy has precipitated an unprecedented demand for efficient electrochemical energy storage systems. Spanning a broad spectrum from consumer electronics, electric mobility, and stationary grid storage to specialized sectors, such as aerospace, medical devices, and industrial robotics, lithium-ion batteries (LIBs) have emerged as the benchmark technology for high-energy-density applications [1–5]. Over the past three decades, the energy density of commercial LIBs has more

than tripled, evolving from approximately 100 Wh kg^{-1} to over 300 Wh kg^{-1}. Despite these advances, the demand for higher energy capacity, fast-charging capabilities, and cost reduction necessitate further breakthroughs in materials science [6–8]. Among the fundamental components of a battery cell, the cathode material represents the critical technological bottleneck, as it dictates the cell's capacity and thermal stability, and it accounts for the largest fraction of the overall cost [9].

Layered transition metal oxides with the general formula $LiNi_xMn_yCo_zO_2$ (NMC, where x + y + z = 1) are currently one of the most promising candidates for next-generation cathodes due to their high specific discharge capacity and established manufacturing scalability. To maximize energy density, research efforts have increasingly focused on Ni-rich compositions ($x \geq 0.8$). Increasing the nickel content significantly elevates the reversible discharge capacity and reduces reliance on cobalt, a critical raw material plagued by high costs, supply chain volatility, and ethical concerns regarding its extraction [10,11]. Consequently, pushing the nickel content toward 90% (NMC90) is a strategic priority for the industry. However, a higher amount of Ni leads to intrinsic structural and chemical instabilities, decreasing cycle life and safety. The rapid capacity fading in Ni-rich cathodes is attributed to a synergistic interplay of several degradation mechanisms. First, the highly reactive Ni^{4+} species formed at high states of charge (SoC) tend to oxidize the liquid electrolyte, leading to the formation of a thick, resistive cathode electrolyte interphase (CEI) [12,13]. Second, these materials undergo severe anisotropic volume changes during cycling, specifically during the H2 → H3 phase transition near 4.2 V. The resulting mechanical strain induces the formation of intergranular microcracks, which electrically isolate primary particles and expose fresh surfaces to further parasitic reactions with the electrolyte [14,15]. Furthermore, during charging (delithiation), the thermodynamic instability of surface Ni^{4+} ions induces a reduction in these species to Ni^{2+}. This process is accompanied by oxygen evolution from the lattice to maintain charge neutrality, which leads to oxygen-assisted decomposition of the electrolyte solvent (e.g., $C_3H_4O_3(EC) + [O] \rightarrow CO_2 + CO + 2H_2O$). This chemical cascade facilitates the hydrolysis of the electrolyte salt, generating hydrofluoric acid ($LiPF_6 + H_2O \rightarrow POF_3 + 2HF + LiF; POF_3 + H_2O \rightarrow HF + HPO_2F_2$), which subsequently promotes transition metal dissolution [16]. Such interfacial instability triggers a structural reconstruction of the layered rhombohedral phase to spinel-like and disordered rock-salt phases, creating a significant kinetic barrier for lithium-ion diffusion. Due to the similar ionic radii of Li^+ (76 pm) and Ni^{2+} (69 pm), Ni^{2+} ions readily migrate into the Li layers. This cation mixing effectively clogs the 1D diffusion channels and renders Li sites electrochemically inactive, further decreasing reversible capacity [15,17–19]. To reduce cation mixing during synthesis, lithium is typically provided in excess. However, this strategy leads to the formation of residual surface species such as LiOH and Li_2CO_3 upon exposure to ambient air, as Ni-rich powders are highly sensitive to moisture and CO_2 [17,20].

To mitigate these drawbacks, various surface engineering strategies, such as cation doping and surface coating, have been extensively investigated. While doping stabilizes the bulk lattice and coatings protect the surface, neither approach fully resolves the trade-off between capacity and stability [9,13,21–23]. A more sophisticated strategy involves the construction of core–shell architectures. This design aims to combine the best attributes of two different compositions: a high-capacity Ni-rich core (e.g., NMC90) encapsulated by a chemically stable, Mn-rich shell (e.g., NMC622). The shell acts as a physical shield, isolating the reactive core from the electrolyte and suppressing the aggressive surface chemistry, while the core provides the necessary energy density [15,24–28].

However, the practical implementation of core–shell cathodes is often hindered by the instability of the interface itself. During the high-temperature calcination process required for synthesis, uncontrolled cation interdiffusion occurs between the core and the shell. This

leads to a blurring of the phase boundary and a dilution of the shell's protective properties. Furthermore, the lattice mismatch between different NMC compositions can induce interfacial strain, leading to delamination during long-term cycling [29–32]. Therefore, engineering a robust interface that suppresses transition metal migration while maintaining high lithium transport is crucial for the success of core–shell materials.

In this context, tungsten has emerged as a highly effective interfacial modifier. Upon synthesis, tungsten forms chemically resilient WO_3 and $Li_xW_yO_z$ species that protect the cathode from hydrofluoric acid (HF)-induced degradation. Beyond surface passivation, $Li_xW_yO_z$ infiltrates the primary particle grain boundaries, acting as a mechanical adhesive that prevents intergranular cracking. Moreover, the doping of the surface lattice with W-ions provides a stabilizing effect, suppressing deleterious phase transitions and maintaining the long-term structural integrity of the material [33–36].

In this work, we present a novel approach to fabricate a robust core–shell architecture featuring a $LiNi_{0.9}Mn_{0.05}Co_{0.05}O_2$ (NMC90) core and a $LiNi_{0.6}Mn_{0.2}Co_{0.2}O_2$ (NMC622) shell, separated by a functional tungsten oxide interlayer. Unlike conventional co-precipitation methods that rely on hydroxide precursors and require complex ammonia chelating agents, an oxalate-assisted co-precipitation route was employed. A distinctive feature of the suggested synthesis is the integration of lithium directly into the precursor solution prior to precipitation and solvent evaporation. This one-pot lithiation strategy avoids the inhomogeneity issues often associated with solid-state mixing of lithium salts [17]. It is hypothesized that the introduction of the tungsten oxide interlayer not only suppresses the interdiffusion of transition metals between the core and the shell during calcination but also strengthens the mechanical integrity of the particle against microcracking. This study provides a comprehensive characterization of the tungsten oxide-modified core–shell cathode material and the resulting electrochemical performance, demonstrating a pathway toward high-energy, long-life cathode materials.

2. Materials and Methods

The following chemicals were purchased and used for the synthesis of the tungsten oxide modified core–shell structured NMC material: nickel (II) acetate tetrahydrate ($Ni(CH_3COO)_2{\cdot}4H_2O$, 99%, ChemPUR, Karlsruhe, Germany), manganese (II) acetate tetrahydrate ($Mn(CH_3COO)_2{\cdot}4H_2O$, ≥99%, Carl Roth, Karlsruhe, Germany), cobalt (II) acetate tetrahydrate ($Co(CH_3COO)_2{\cdot}4H_2O$, ≥98%, Carl Roth), lithium acetate ($LiCH_3COO$, ≥99%, Carl Roth), oxalic acid dihydrate ($C_2H_2O_4{\cdot}2H_2O$, ≥99%, Carl Roth), ammonium tungstate ($(NH_4)_{10}H_2(W_2O_7)_6$, +99.99%, Thermo Fisher, Waltham, MA, USA), isopropanol (C_3H_8O, technical grade, Thermo Fisher).

For electrode preparation, polyvinylidene fluoride (PVDF, 99.9%, Thermo Fisher) and N-methyl-2-pyrrolidone (NMP, ≥99.5%, Thermo Fisher) were used as binder and solvent, respectively. Activated carbon (C, p.a., Carl Roth) served as a conductive additive.

For coin cell assembly, lithium metal chips (16 mm diameter, Nanografi, Ankara, Türkiye) were used as counter and reference electrodes. A glass fiber filter (Whatman GF/D, Cytiva, Marlborough, MA, USA) was used as a separator, and a 1 M $LiPF_6$ solution in ethylene carbonate/dimethyl carbonate (EC/DMC = 50/50 (*v*/*v*), battery grade, Merck, Darmstadt, Germany) was used as an electrolyte.

2.1. Material Synthesis of NMC90 Core

The synthesis of NMC90 core particles via the oxalic acid-assisted co-precipitation route is illustrated in Figure 1. Nickel (II) acetate (0.9 mol), manganese (II) acetate (0.05 mol), and cobalt (II) acetate (0.05 mol) were dissolved separately in deionized water and subsequently combined to form a homogeneous transition metal (TM) precursor solution.

Acetate salts were specifically selected over sulfates to avoid sulfur contamination in the final product, as the resulting acetic acid is volatile and easily removed during thermal treatment. Based on preliminary optimization experiments, a Li:TM molar ratio of 1.5:1 yielded the most promising results regarding phase purity, crystallinity, and processability. Higher concentrations of lithium led to an increased hardness of the synthesized powders, which made effective grinding difficult. Therefore, 1.5 mol of lithium acetate was dissolved and added to the mixture to compensate for lithium volatilization during the high-temperature calcination process. The precursor solution was maintained at 65 °C under continuous stirring at 350 rpm. Oxalic acid (1.75 mol), serving as the precipitating agent, was added dropwise to the mixture. Since oxalic acid acts as both a precipitating agent and a complexing agent, which stabilizes the oxidation state of the transition metals, further pH control or synthesis under an inert atmosphere is not necessary. After adding oxalic acid, the suspension was kept at 65 °C under stirring for 1 h. Due to the solubility of the formed lithium oxalate, the solvent was removed via evaporation at 80 °C rather than filtration to maintain the ratio of substances. The resulting precipitate was dried overnight in an oven at 80 °C. The dried powder was calcined at 850 °C for 8 h with a heating ramp of 3 °C/min. The final calcined powder was ground in a mortar to eliminate agglomerates.

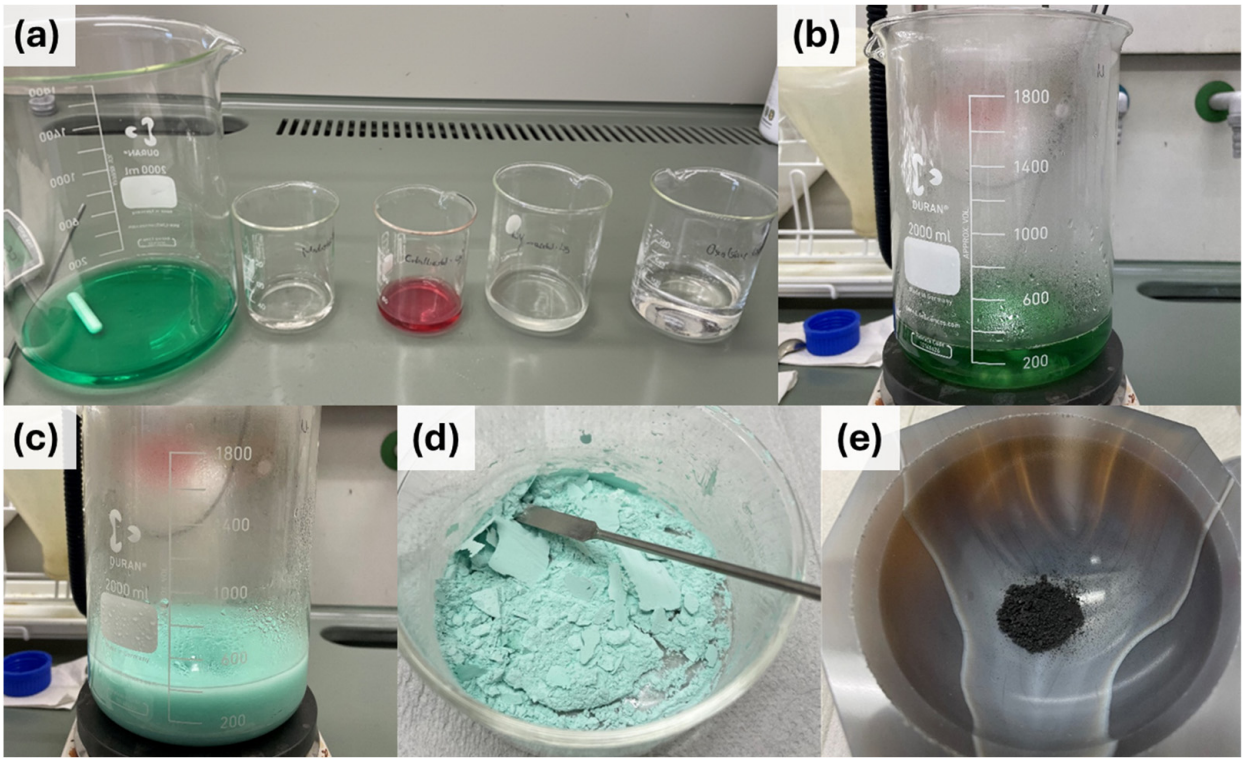

Figure 1. Synthesis process for NMC via the oxalate co-precipitation route. (**a**) Preparation of precursor solutions by separately dissolving TM salts, lithium salt, and oxalic acid. (**b**) Controlled mixing and homogenization of the reactants at 65 °C under continuous stirring. (**c**) Formation of the metal-oxalate precipitate following the dropwise addition of oxalic acid. (**d**) Intermediate product obtained as a fine greenish powder after drying at 80 °C overnight, and (**e**) final NMC powder after calcination at 850 °C for 8 h and subsequent mortar grinding for de-agglomeration.

2.2. Coating of NMC90 Core with Tungsten Oxide

To apply the tungsten oxide coating, ammonium tungstate (1 wt%) was dissolved in isopropanol. The previously synthesized NMC90 powder was dispersed in this solution. The suspension was stirred continuously at 70 °C to facilitate solvent evaporation. Follow-

ing the removal of isopropanol, the resulting powder was calcined at 650 °C for 4 h with a heating rate of 3 °C/min to form a stable tungsten oxide coating on the NMC90 core.

The reaction is as follows [37]:

$$24LiOH + (NH_4)_{10}H_2(W_2O_7)_6 \rightarrow 12Li_2WO_4 + 10NH_3 + 18H_2O$$

$$(NH_4)_{10}H_2(W_2O_7)_6 \xrightarrow{\Delta T} 12WO_3 + 10NH_3 + 6H_2O$$

2.3. Synthesis of NMC622 Shell on Tungsten Oxide-Coated Core Particles

Following the coating of a tungsten oxide layer onto the NMC90 core particles, an outer shell of NMC622 was synthesized using the procedure described in Section 2.1 with adjusted molar ratios. Nickel (II) acetate, manganese (II) acetate, and cobalt (II) acetate were dissolved in deionized water in a molar ratio of 6:2:2. The tungsten oxide-coated NMC90 powder was dispersed directly into this metal precursor solution. Oxalic acid was subsequently added dropwise to induce co-precipitation of the NMC622 shell onto the suspended particles. The solvent was then evaporated, and the precipitate dried and calcined following the same thermal parameters used for the core synthesis.

2.4. Structural and Morphological Characterization

The crystallographic structure of the synthesized powders was analyzed by X-ray diffraction (XRD) using a Bruker D8 Advance diffractometer (Bruker, Bremen, Germany) equipped with Cu Kα radiation (λ = 1.5406 Å). Patterns were recorded in continuous scanning mode over a 2θ range of 10–90° with a step size of 0.024°, operating at 35 kV and 30 mA. Rietveld refinement was performed on the diffraction data using TOPAS (Version 6, Bruker AXS, Karlsruhe, Germany) to determine precise lattice parameters and to identify potential secondary phases.

Particle morphology was examined using a Zeiss Ultra 55 scanning electron microscope (SEM; Zeiss, Jena, Germany) at an accelerating voltage of 8 kV. The elemental composition and spatial distribution were analyzed via energy-dispersive X-ray spectroscopy (EDS) integrated into the SEM system, operating at 15 kV.

For further surface analysis of the tungsten oxide-coated NMC90 particles, a Thermo Fisher Nexsa G2 (Thermo Fisher Scientific, East Grinstead, UK)surface analysis system was used. X-ray photoelectron spectroscopy (XPS) was employed to determine the surface oxidation states and chemical composition, and ion scattering spectroscopy (ISS) was performed using He^+ ions to probe the outermost surface layers, enabling a precise analysis of the chemical environment within a depth range of 1–10 nm.

2.5. Electrochemical Performance

Electrochemical performance was evaluated using coin cells (CR2032 configuration, Nanografi, Ankara, Turkey). Positive electrodes were fabricated from a slurry containing the synthesized NMC powder as the active material, activated carbon as the conductive additive, and polyvinylidene fluoride (PVDF) binder in an 8:1:1 mass ratio. To prepare the slurry, PVDF was dissolved in N-methyl-2-pyrrolidone (NMP) at 60–65 °C under stirring. Upon cooling to room temperature, activated carbon and the active material were added. The mixture was stirred overnight at 1400 rpm to ensure homogeneity. The resulting slurry was cast onto aluminum foil using a doctor blade with a wet-film thickness of 450 µm and dried at 70 °C for 4 h, resulting in a dry coating thickness of 100 µm. Circular electrodes of 14 mm diameter were punched from the dried electrode. Cell assembly was conducted in an argon-filled glovebox. Galvanostatic charge–discharge (GCD) cycling was performed at room temperature using a constant current of C/10 within a voltage window of 2.7–4.2 V for the initial formation cycles. Electrochemical impedance spectroscopy (EIS) was conducted

on the assembled cells to evaluate charge-transfer resistance and ion-transport kinetics at the electrode-electrolyte interface.

3. Results and Discussion

3.1. Structural Characterization with XRD

XRD was employed to investigate the crystal structures of the synthesized NMC materials. Patterns were collected from the pristine NMC90, the tungsten oxide-coated NMC90 (hereafter referred to as NMC90-W), and, as a reference, a self-synthesized NMC622. These samples are compared to the pattern of the core–shell structured NMC with a tungsten oxide interlayer (referred to as core–shell–W) in Figure 2. As can be seen in Figure 2a, the patterns look almost the same and comply with the reference spectra for $LiNi_{0.8}Mn_{0.1}Co_{0.1}O_2$ (JCPDS 00-066-0856). Only around 21° and 32° are some small peaks visible, which belong to Li_2CO_3 [38]. These peaks are more pronounced in the NMC90 sample compared to NMC622 and core–shell–W, likely due to the increased moisture sensitivity associated with higher nickel content. The peak intensity ratios of (003) and (104) were calculated and are summarized in Table 1. For all samples, the ratio is higher than 1.2, indicating a low Li^+/Ni^{2+} cation mixing [16,39–42]. Furthermore, splitting of the (006)/(102) (Figure 2b) and (018)/(110) (Figure 2c) peaks is clearly visible for all samples. This splitting implicates a well-defined α-$NaFeO_2$ hexagonal structure belonging to the $R\bar{3}m$ space group [43–45]. The Rietveld refinement further confirms a highly ordered layered structure, as evidenced by a c/a ratio of over 4.9 [46,47].

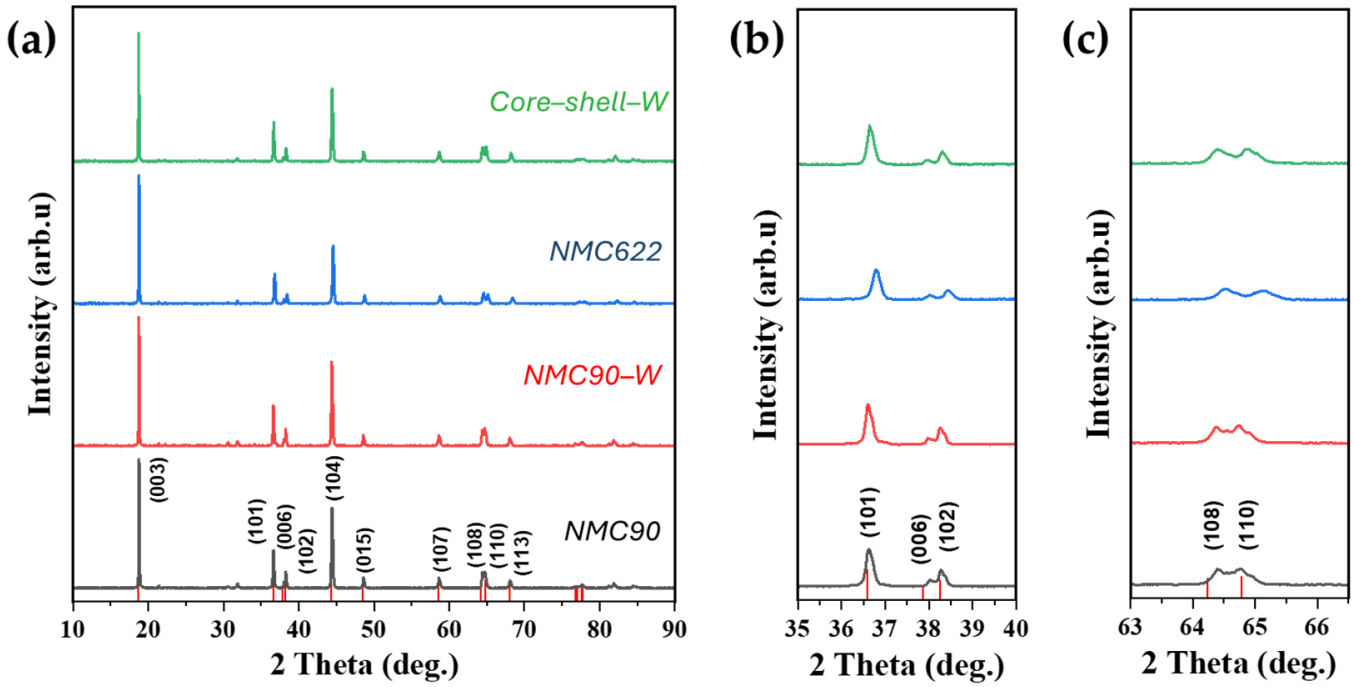

Figure 2. XRD of NMC90, tungsten oxide-coated NMC90 (NMC90-W), NMC622 and core–shell structured NMC with a tungsten oxide interlayer (core–shell–W), (**a**) overall pattern, (**b**) (101) and the double peaks (006) and (102), (**c**) double peak (108) and (110); Color coding in (**b**,**c**) is the same as in (**a**). Reference peaks from $LiNi_{0.8}Mn_{0.1}Co_{0.1}O_2$ (JCPDS 00-066-0856).

Table 1. Rietveld refinement results of the XRD data for NMC90, tungsten oxide-coated NMC90, NMC622, and core–shell structured NMC.

	NMC90	NMC90-W	NMC622	Core–Shell–W
I(003)/I(104)	1.61	1.53	1.95	1.34
a = b (Å)	2.8779	2.8749	2.8665	2.8745
c (Å)	14.1921	14.2173	14.2082	14.2238
c/a	4.9314	4.9452	4.9566	4.9482
R_{wp} (%)	5.66	5.74	6.49	6.15
GOF (%)	1.27	1.28	1.22	1.15

Regarding the tungsten oxide coating, no WO_3 or Li_2WO_4 phases were detected in the XRD patterns, suggesting that the coating amount is below the detection limit [48]. Additionally, c/a ratios are similar for all samples, which indicates that there is no integration of the tungsten ions into the crystal lattice [47,49]. The low R_{wp} and GOF values confirm the reliability of the Rietveld refinement.

3.2. Morphological Characterization (SEM and EDS)

The morphological characteristics of the samples were investigated via SEM, as presented in Figure 3. Figure 3a–c displays the pristine NMC90 and the uncalcined and calcined NMC90-W, respectively. Figure 3d shows the pristine NMC622, while Figure 3e,f represents the core–shell samples without (further labeled as core–shell) and with a tungsten oxide interlayer. As observed in Figure 3a, the NMC90 secondary particles exhibit an angular rather than spherical morphology. Small and bright-colored particles are visible on the surface, likely corresponding to Li_2CO_3 residues, which aligns with the previously discussed XRD results. Following the tungsten oxide coating process (Figure 3b), a dense layer of fine particles is distributed across the NMC90 surface, indicating high coating coverage. These surface features largely disappear after calcination (Figure 3c), resulting in a smoother, less angular particle surface. In contrast, the pristine NMC622 (Figure 3d) consists of smaller primary particles and exhibits a more spherical secondary morphology, consistent with prior reports [50]. Furthermore, there is a notable absence of small, brighter-colored surface residues, which again correlates with the XRD data. core–shell structured particles (Figure 3e,f) appear morphologically identical, with no significant differences in size or shape. Compared to the single-composition NMC90 and NMC622, core–shell particles are significantly larger, more spherical, and nearly without surface residues. To assess the overall sample homogeneity and particle size distribution, low-magnification SEM images are provided in Figure S1. While the pristine NMC90 exhibits a broader size distribution with finer particles alongside larger irregular agglomerates, the tungsten-coated and core–shell samples consist predominantly of coarser secondary structures. It should be noted that while NMC90 and NMC622 were processed in a mortar, the coated and core–shell samples were not subjected to intensive milling to preserve the structural integrity of the tungsten oxide interlayer and the core–shell architecture.

To evaluate the homogeneity of the tungsten oxide coating on the NMC90, EDS was performed. The elemental mapping in Figure 4 confirms a uniform distribution of W across the NMC90 surface, alongside the homogenous distribution of Ni, Co, and Mn throughout the particle [51].

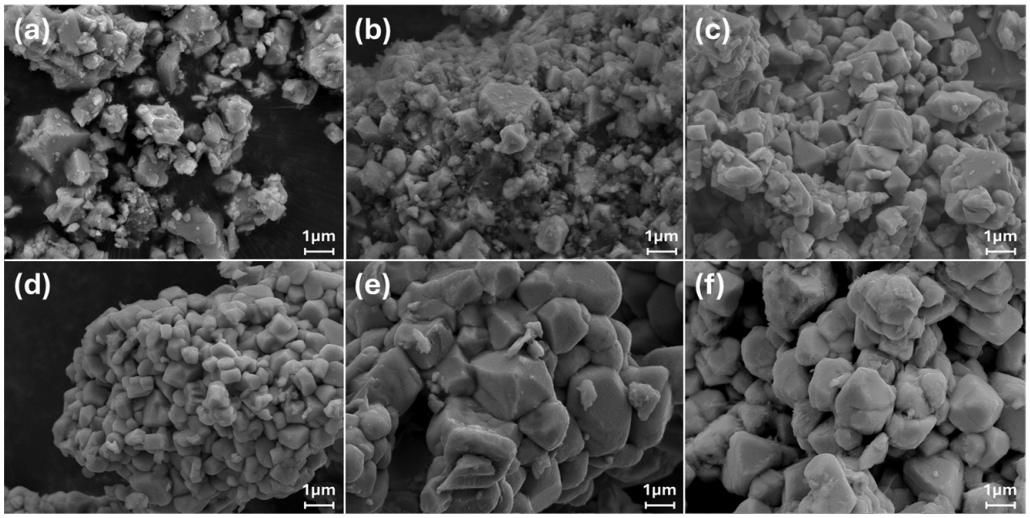

Figure 3. SEM images of the synthesized samples: (**a**) NMC90; (**b**) NMC90-W—uncalcined; (**c**) NMC90-W—calcined; (**d**) NMC622; (**e**) core–shell; (**f**) core–shell–W.

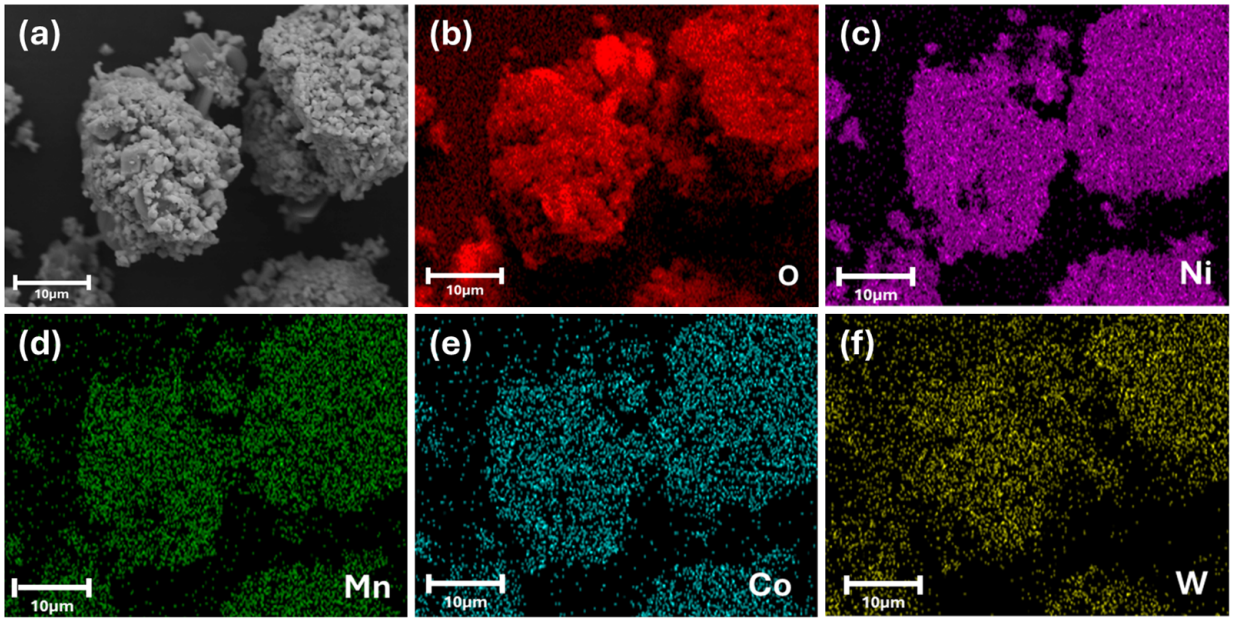

Figure 4. EDS elemental mapping of NMC90-W secondary particles. (**a**) SEM micrograph of a representative particle. (**b**–**f**) Corresponding EDS maps for O, Ni, Mn, Co, and W, respectively. The overlapping elemental signals demonstrate a uniform distribution of tungsten species across the cathode surface.

3.3. XPS and ISS Spectra

Since EDS provides information from the bulk and underlying particles due to its large interaction volume, XPS and ISS were employed to selectively analyze the surface of the NMC90 and NMC90-W particles. XPS characterizes the chemical bonding and electronic configurations, while ISS provides sensitivity to the topmost atomic layers, which is particularly advantageous for detecting thin surface coatings like tungsten oxide. In Figure 5a, the survey scan of pristine NMC90 reveals the presence of residual contaminants such as Na, S, N, and F, likely introduced during processing and handling. More significantly, the high-resolution spectra of O 1s, C 1s, and Li 1s (Figure 5b–d) indicate a substantial amount of Li_2CO_3 on the surface. This is attributed to the calcination process in air. As high-nickel NMC materials are highly sensitive to ambient moisture and CO_2, the formation of Li_2CO_3

is a common degradation mechanism. The literature suggests that Li_2CO_3 promotes parasitic reactions and electrolyte decomposition, particularly at high voltages, involving lattice oxygen from the NMC structure. This process is often accompanied by the reduction of Ni^{3+} to Ni^{2+}. The resulting surface reconstruction into a rock-salt-like phase (similar to NiO or disordered $LiNiO_2$) is electrochemically inactive and hinders lithium-ion diffusion, leading to performance fading [52,53]. The Ni 2p spectra (Figure 5e) were also examined to further evaluate the surface state. The two primary peaks, Ni 2p3/2 and Ni 2p1/2, are located at ≈855 eV and ≈873 eV, respectively. These are accompanied by satellite peaks located at ≈862 eV and ≈879 eV. These satellite peaks generally arise from multiple splittings in the energy levels of the transition metal ions and serve as a characteristic indicator for the presence of divalent nickel (Ni^{2+}) at the surface [47,54].

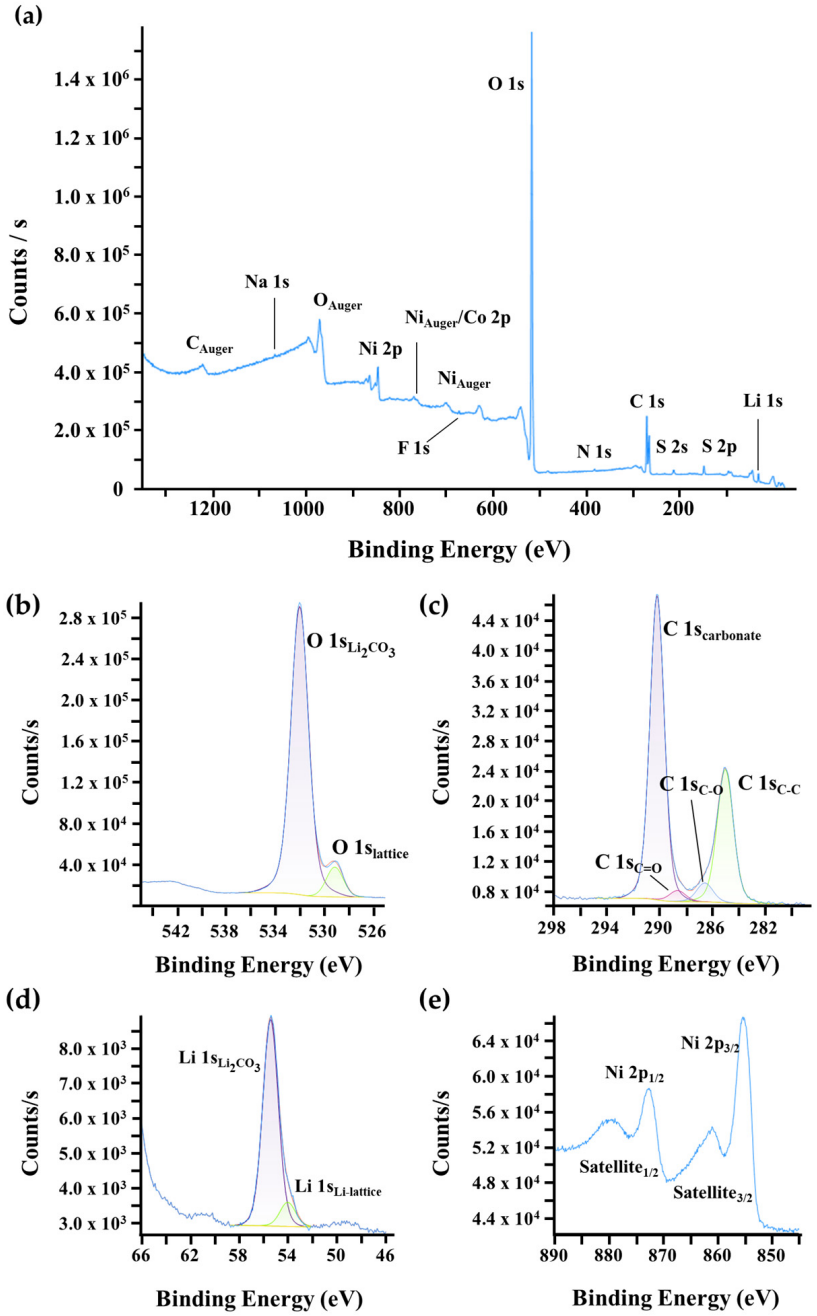

Figure 5. XPS surface characterization of pristine NMC90. (**a**) Wide-scan survey spectrum and high-resolution core-level spectra of (**b**) O 1s, (**c**) C 1s, (**d**) Li 1s, and (**e**) Ni 2p regions.

For the coated NMC90-W sample, the XPS survey shows new characteristic peaks for tungsten in Figure 6a, while the intensities of the O 1s, C 1s, and Li 1s signals associated with Li_2CO_3 are lower compared to the uncoated sample. This suggests that the coating process may consume surface residuals through the reaction of tungsten with lithium and oxygen to form Li_2WO_4 or WO_3 phases. The tungsten signal consists of the W 5p peak at approximately 41 eV and the well-resolved W 4f doublet, located at ≈36 eV (W $4f_{7/2}$) and ≈38 eV (W $4f_{5/2}$). The absence of additional shoulders and the sharp peak shapes indicate that tungsten exists only in the +6 oxidation state, consistent with WO_3 or Li_2WO_4. Although Li_2WO_4 typically has a Li 1s peak at 56 eV, the presence of Li_2CO_3 results in an overlap, preventing a definitive classification based on the lithium signal alone. This aligns with findings by Animesh Dutta et al. and other studies [37,47,55,56].

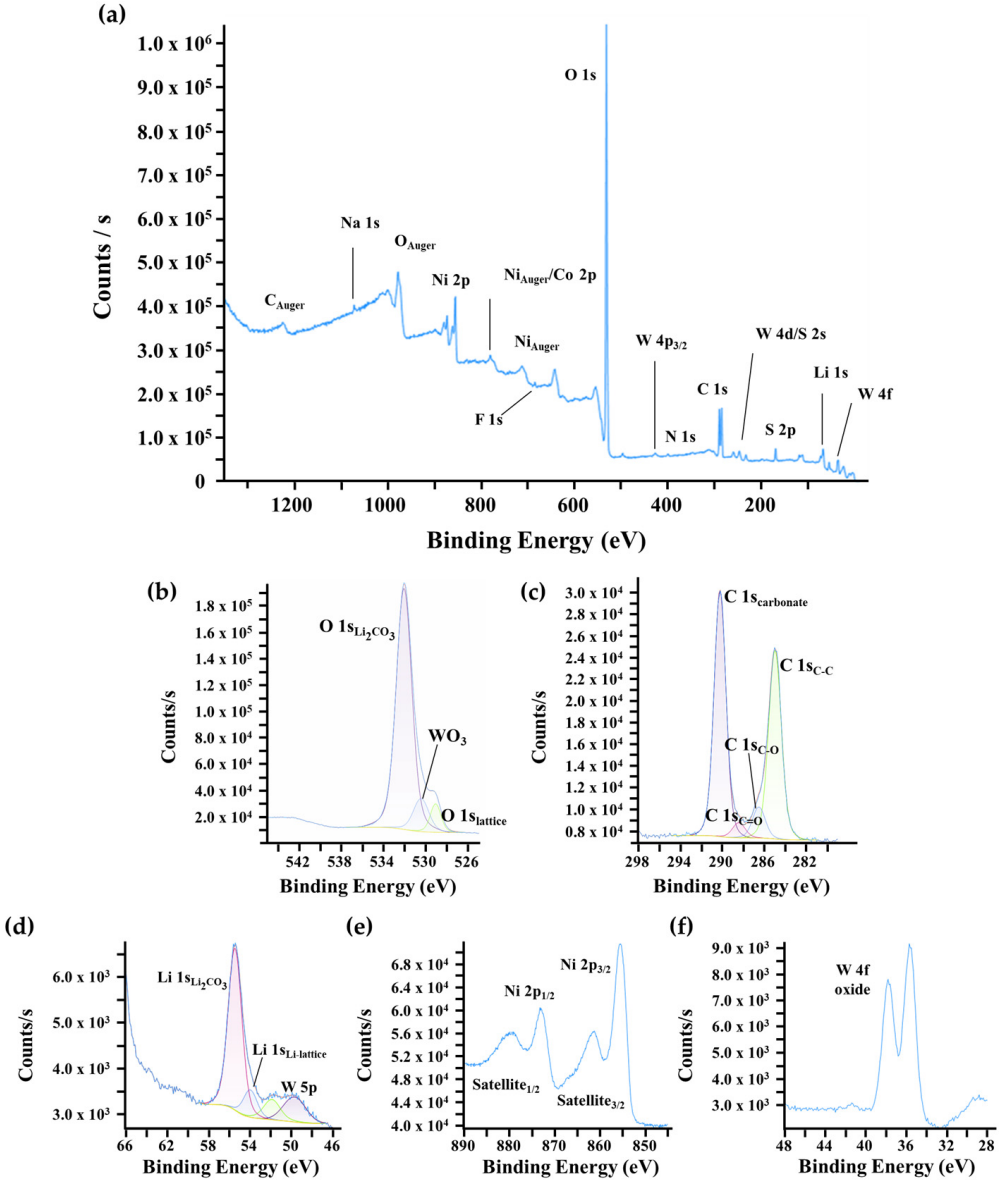

Figure 6. XPS surface characterization of coated NMC90-W. (**a**) Wide-scan survey spectrum and high-resolution core-level spectra of (**b**) O 1s, (**c**) C 1s, (**d**) Li 1s, (**e**) Ni 2p regions, and (**f**) W 4f.

Figure 7 displays the ISS spectra for the pristine NMC90 and the tungsten-coated NMC90-W samples. The two spectra are nearly identical. However, the NMC90-W sample exhibits an additional distinct peak at approximately 875 eV, which is assigned to tungsten. This observation correlates with the EDS data, further supporting the presence of tungsten

at the surface of the cathode particles. Notably, the characteristic peaks for Ni, Co, and Mn remain clearly visible in the NMC90-W spectrum. Due to the high sensitivity of ISS, which selectively probes only the topmost 1–2 atomic layers, the continued visibility of the transition metals indicates that the tungsten-based layer does not form a complete, thick encapsulation. Instead, this suggests the coating is either ultra-thin or characterized by an island-like, inhomogeneous distribution across the particle surface. Ideally, a thin and homogeneous coating is favored to provide uniform surface protection while maintaining low interfacial resistance for fast kinetics. However, achieving perfect, pinhole-free coverage is often difficult via standard dry or wet coating methods. Alternatively, an island-like distribution acts as a partial physical barrier, which ensures facile Li^+ transport through uncoated regions. Studies suggest that full coverage is not always necessary for performance gains. These discrete clusters can effectively stabilize the surface structure and enhance electrochemical durability, as further evaluated by the following electrochemical characterization [57–59].

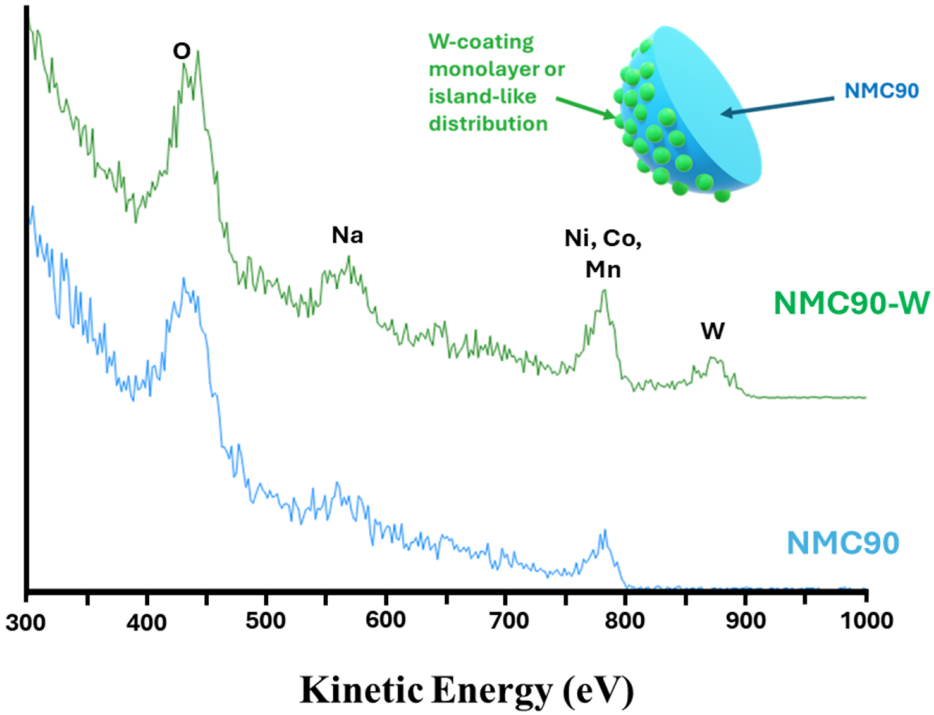

Figure 7. ISS spectra of pristine NMC90 and NMC90-W and a schematic illustration of the tungsten-coated NMC90 particle.

3.4. Galvanostatic Charge and Discharge Measurements

The GCD profiles for NMC90, NMC622, and the core–shell structured NMC samples, both with and without a tungsten oxide coating, are illustrated in Figure 8a–d, while the corresponding specific discharge capacities and coulombic efficiencies after the first and fifth cycles are summarized in Table 2. Notably, pure NMC90 exhibited a relatively low specific discharge capacity of 81.7 mAh/g compared to the other samples. The initial open-circuit voltage (OCV) was measured below 2.7 V, leading to the start of the first charging cycle in the graph at 30 mAh/g. A prolonged duration was observed during the initial cycle to reach the 4.2 V cutoff voltage, which is attributed to the formation of the solid electrolyte interphase (SEI) and the associated consumption of lithium ions (Figure 8a). Consequently, the initial coulombic efficiency (CE) in the first cycle is lower, primarily due to this SEI formation. Specifically, NMC90 exhibits a significantly lower CE compared to the other materials, as can be seen in Table 2, which can be attributed to its higher

surface reactivity. In contrast, the core–shell materials show improved CEs, demonstrating their enhanced structural and interfacial stability. While subsequent cycles demonstrated consistent charge–discharge behavior, the overall capacity remained significantly lower than values typically reported in the literature for high-nickel materials. This capacity limitation may be attributed to the presence of surface Li_2CO_3, which was already observed in the XRD, SEM, and XPS measurements. This impurity leads to the formation of an electrochemically inactive reconstruction layer on the NMC particles, which hinders the lithium-ion transport and increases the interfacial resistance, leading to a reduction in capacity [60]. Interestingly, pure NMC622 showed a higher specific discharge capacity of 118.5 mAh/g (Figure 8b) compared to NMC90 (Figure 8a). This observation deviates from the expected trend, as higher nickel concentrations generally yield higher capacities in the literature [61]. The core–shell architecture outperformed both individual NMC components, achieving a capacity of 138.2 mAh/g (Figure 8c), whereas core–shell–W showed a slightly lower value of 136.9 mAh/g (Figure 8d). This minor difference may be attributed to the synergistic effect of the active materials composed of NMC90 as core, NMC622 as shell, and tungsten oxide as interlayer between core and shell. By the fifth cycle, all samples reach a high CE, indicating successful stabilization of the material and highly reversible lithiation/delithiation processes. Across all samples, the coulombic efficiency remained high, generally ranging between 98% and 100%, indicating good electrochemical reversibility following the initial stabilization phase.

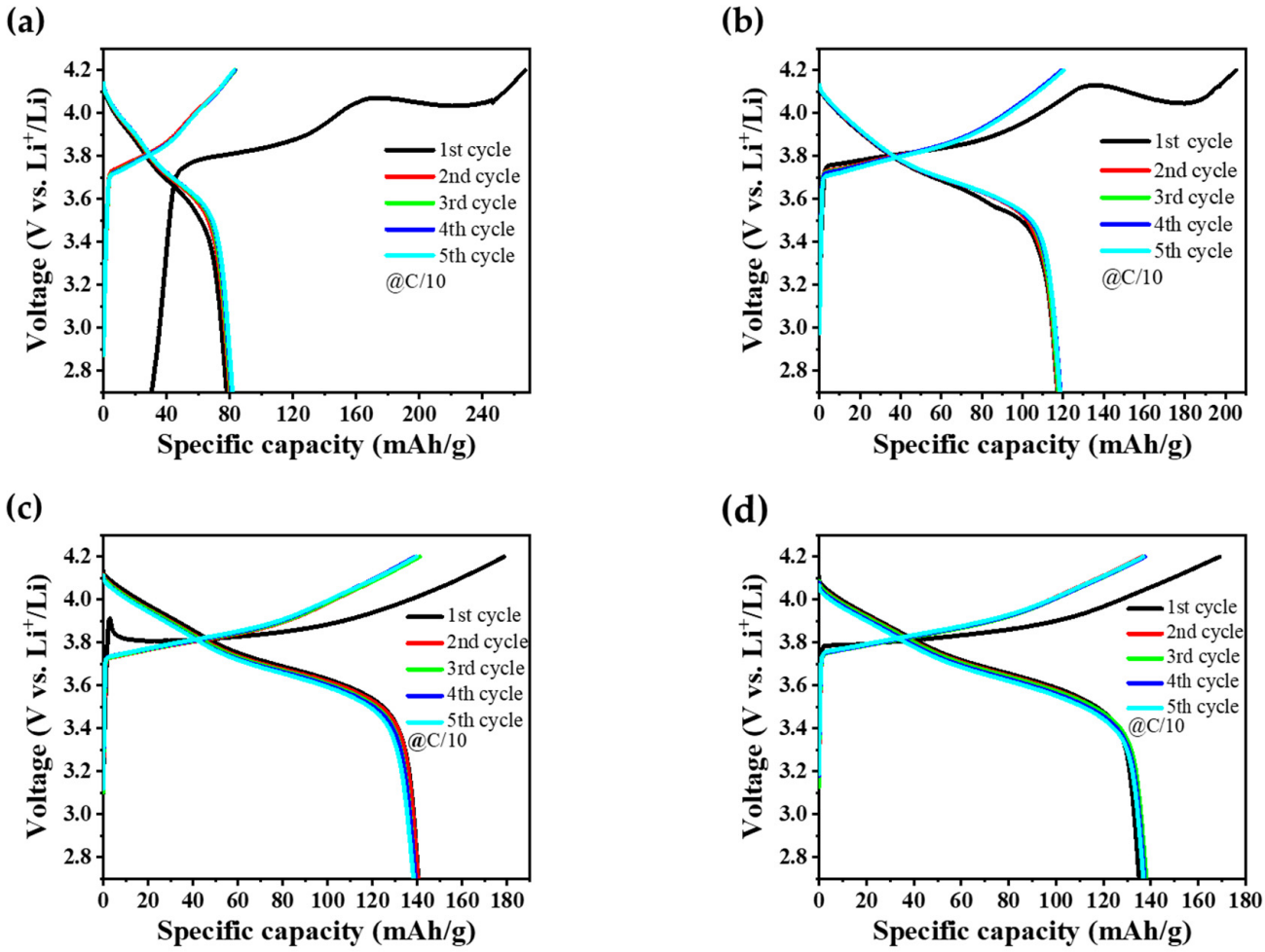

Figure 8. GCD curves of the initial five cycles performed at C/10 within a potential window of 2.7–4.2 V for (**a**) NMC90, (**b**) NMC622, (**c**) core–shell, and (**d**) core–shell–W cathode electrodes.

Table 2. Discharge capacity and Coulombic efficiency values after the 5th cycle for pristine NMC90, pristine NMC622, core–shell, and core–shell–W.

	NMC90		**NMC622**		**Core–Shell**		**Core–Shell–W**	
	1st Cycle	5th Cycle	1st Cycle	5th Cycle	1st Cycle	5th Cycle	1st Cycle	5th Cycle
Specific discharge capacity (mAh/g)	78.0	81.7	117.21	118.5	140.4	138.2	135.1	136.9
Coulombic efficiency (%)	29.2	98.8	57.1	98.5	78.6	98.5	79.9	100

3.5. Cycling Stability Measurements of Core–Shell with and Without Tungsten Oxide Coating

The long-term cycling stability of the core–shell samples, with and without a tungsten oxide coating, was evaluated over 50 cycles between 2.7 and 4.2 V at a rate of C/10 (Figure 9). The results demonstrate that the tungsten oxide coating significantly enhances the cyclability of the cathode material, effectively doubling its operational lifespan. Specifically, the tungsten oxide-coated sample maintained an 80% state of health (SoH) until the 44th cycle, whereas the uncoated core–shell sample reached this degradation threshold by the 20th cycle. These results indicate that the tungsten oxide interlayer exerts a stabilizing effect beyond simple surface protection. This synergistic enhancement likely originates from the suppression of detrimental side reactions at the core–shell interface and a reduction in mechanical strain during lithiation/delithiation cycles. Furthermore, the tungsten species may act as a structural buffer, preventing cation disordering and maintaining the integrity of the core–shell architecture. Additionally, the core–shell design provides a higher specific discharge capacity than the individual core or shell materials, while the tungsten oxide modification acts as a critical protective layer that mitigates capacity fade and improves structural longevity during electrochemical cycling.

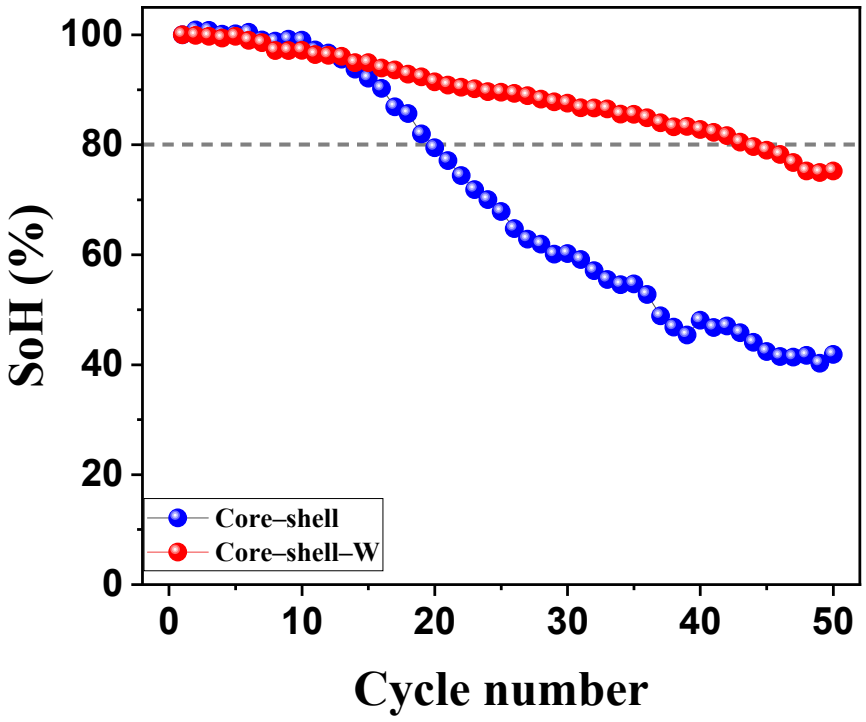

Figure 9. Long-term cycling stability of core–shell NMC cathode powders without and with a tungsten oxide interlayer. Cycling was performed between 2.7 and 4.2 V with C/10.

3.6. EIS Analysis

Figure 10 illustrates EIS Nyquist plots for the core–shell samples without and with a tungsten oxide interlayer after the 50th cycle. The pristine core–shell sample (Figure 10a) exhibits impedance in the Mega-Ω range, accompanied by significant scattering of the data points. In contrast, the core–shell–W sample (Figure 10b) remains in the lower kilo-Ω range and displays a discernible semicircular arc. Although the arc is not clearly resolved, it represents a substantial reduction in the charge–transfer resistance (R_{ct}) compared to the extreme impedance observed in the core–shell material without a tungsten oxide interlayer. This indicates that the tungsten oxide interlayer significantly facilitates charge transfer at the core–shell interface. The impedance rise in the core–shell material without a tungsten oxide interlayer is likely triggered by the formation of an insulating surface reconstruction layer (e.g., rock-salt phase) and the accumulation of decomposition products [62]. Furthermore, the ohmic resistance R_s representing the resistance of the electrolyte, current collector contacts, and bulk electrode, was measured at 22.3 kΩ for the pristine core–shell and 35.3 Ω for core–shell–W. The excessively high R_s in the unmodified sample suggest a near-total loss of electrical contact or severe electrolyte depletion [62,63]. In the lower frequency range, the characteristic straight line corresponds to the Warburg impedance (Z_w), which describes the solid-state diffusion of Li^+ ions within the cathode bulk [62–64]. While the core–shell–W sample shows a more defined diffusion tail, it also exhibits increased scattering and a rise into the MΩ range at very low frequencies. This suggests that while the tungsten interlayer improves interfacial kinetics, lithium-ion diffusion remains a limiting factor after extended cycling. After all, the fact that core–shell–W maintains a significantly lower and more stable impedance confirms that the tungsten interlayer effectively preserves conductive pathways and mitigates the drastic surface degradation that plagues the core–shell material without a tungsten oxide interlayer.

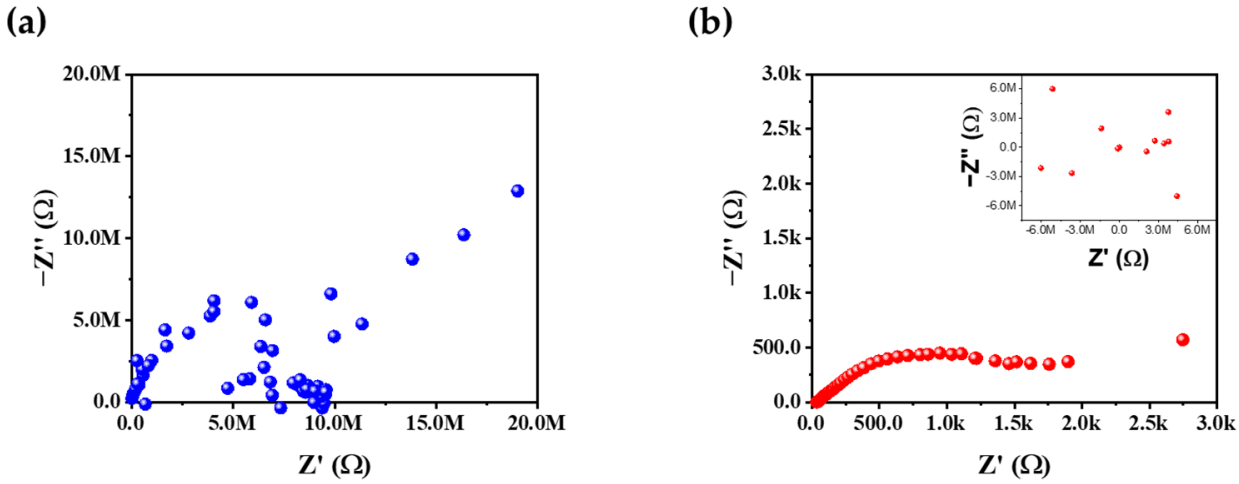

Figure 10. EIS after 50 cycles of (**a**) core–shell and (**b**) core–shell with a tungsten oxide interlayer, with additional graph, which shows scattering in MΩ for lower frequency.

4. Conclusions

In this study, a core–shell structured NMC cathode with a tungsten oxide interlayer was successfully synthesized via a novel, one-pot co-precipitation method. By utilizing oxalic acid as a precipitant, a more cost-effective and environmentally friendly synthesis route was established compared to conventional hydroxide-based methods. The addition of lithium directly into the reaction solution ensured high chemical homogeneity of the precursor. Structural and morphological characterization confirmed the formation of the desired $R\bar{3}m$ phase and verified the successful integration of tungsten at the interface

between the NMC90 core and NMC622 shell. While ISS measurements suggested that the tungsten oxide coating exists as an ultra-thin or a non-uniform island-like layer, its impact on the electrochemical performance was significant. The tungsten interlayer appears to stabilize the core–shell interface, potentially mitigating structural degradation during long-term cycling. Electrochemical evaluation revealed a significant performance gain with the core–shell architecture, achieving a specific discharge capacity of 138.2 mAh/g, which notably surpasses the capacities of both the pristine NMC90 core (81.7 mAh/g) and the NMC622 shell (118.5 mAh/g). The stability of these materials was further highlighted during cycling, while core–shell–W reached an SoH of 80% at the 44th cycle, whereas the core–shell without a tungsten oxide interlayer reached this threshold by the 20th cycle. This suggests a beneficial synergistic interaction, where the protective shell and the stabilizing interlayer effectively compensate for the inherent limitations of the standalone materials.

Although surface impurities such as Li_2CO_3 initially limited the absolute capacity, future optimizations, for instance, by calcination under an oxygen atmosphere or specialized washing procedures, could effectively remove these species, resulting in further enhancement of the discharge capacity. In conclusion, this work demonstrates that combining a core–shell structure with a functional tungsten oxide interlayer offers a robust strategy for enhancing the structural stability and longevity of high-capacity, nickel-rich cathode materials for next-generation lithium-ion batteries.

Supplementary Materials: The following supporting information can be downloaded at: https://www.mdpi.com/article/10.3390/batteries12030082/s1, Figure S1: XRD patterns of NMC90 with varying lithium content. (a) Overall pattern; (b) (101) and the double peaks (006) & (102); (c) Double peak (108) & (110); Table S1: Comparison of I(003)/I(104) peak intensity ratios for NMC90 samples with different lithium content; Figure S2: SEM images of NMC90 with varying lithium content (1.5, 2 and 2.2 mol). (a,c,e) High-magnification and (b,d,f) low-magnification views of samples with: (a,b) 1.5 mol Li, (c,d) 2 mol Li, and (e,f) 2.2 mol Li; Figure S3: XRD patterns of NMC622 with varying lithium content. (a) Overall pattern; (b) (101) and the double peaks (006) & (102); (c) Double peak (108) & (110).; Table S2: Comparison of I(003)/I(104) peak intensity ratios for NMC622 samples with different lithium content; Figure S4: SEM images of NMC622 with varying lithium content (1.5, 2 and 2.2 mol). (a,c,e) High-magnification and (b,d,f) low-magnification views of samples with: (a,b) 1.5 mol Li, (c,d) 2 mol Li, and (e,f) 2.2 mol Li; Figure S5: XRD patterns comparing two-step and single-step calcination processes for NMC90. (a) Overall pattern; (b) (101) and the double peaks (006) & (102); (c) Double peak (108) & (110). The black curve represents NMC90 after initial calcination at 450 °C (4 h) followed by mortar grinding. The red curve shows the same powder after a second calcination step at 850 °C (8 h). The blue curve represents the single-step calcined NMC90 (850 °C, 8 h). All samples were heated at a rate of 3 °C/min. The I(003)/I(104) intensity ratio is 1.36 for the two-step calcined powder and 1.61 for the single-step calcined powder; Figure S6: SEM images of NMC90 comparing two-step and single-step calcination processes at different magnifications. (a,c,e) High-magnification and (b,d,f) low-magnification views of: (a,d) single step; (b,e) 1st stage of the two-step process; (c,f) 2nd stage of the two-step product; Figure S7: Low-magnification SEM images of the synthesized samples, providing a broader overview of particle morphology for: (a) NMC90; (b) NMC90-W—uncalcined; (c) NMC90-W—calcined; (d) NMC622; (e) Core-shell; (f) Core-shell-W.

Author Contributions: Conceptualization, S.K. and B.S.; methodology, B.T. and S.K.; validation, B.T., S.K., P.S., A.R. and B.S.; formal analysis, B.T.; investigation, B.T. and P.S.; resources, B.S.; data curation, B.T.; writing—original draft preparation, B.T.; writing—review and editing, S.K., A.R. and B.S.; visualization, B.T.; supervision, S.K. and B.S.; project administration, B.S.; funding acquisition, B.S. All authors have read and agreed to the published version of the manuscript.

Funding: This project has received funding from the European Union's research and innovation program Horizon Europe under the grant agreement No. 101103702 (PHOENIX) and the involvement in No. 101104022 (Battery 2030 CSA3). Views and opinions expressed are, however, those of the author(s) only and do not necessarily reflect those of the European Union. Neither the European Union nor the granting authority can be held responsible for them.

Funded by the European Union

Data Availability Statement: Data will be made available on request.

Acknowledgments: XPS and ISS measurements were conducted by Paul Mack from Thermo Fisher Scientific using the Nexsa G2 instrument (Thermo Fisher Scientific, East Grinstead, UK). The authors gratefully acknowledge R. Lontio Fomekong for his valuable suggestions regarding the oxalate route synthesis of the cathode powders.

Conflicts of Interest: The authors declare no conflicts of interest.

References

1. Dev Anand, M.; Sasidharakurup, R.; Mercy, T.; Jacob, T.; Athula Devi, S. Lithium-ion cells for space applications: Aspects of durability. *Adv. Space Res.* **2023**, *72*, 2948–2958. [CrossRef]
2. Pathak, A.D.; Saha, S.; Bharti, V.K.; Gaikwad, M.M.; Sharma, C.S. A review on battery technology for space application. *J. Energy Storage* **2023**, *61*, 106792. [CrossRef]
3. Krause, F.C.; Ruiz, J.P.; Jones, S.C.; Brandon, E.J.; Darcy, E.C.; Iannello, C.J.; Bugga, R.V. Performance of commercial Li-ion cells for future NASA missions and aerospace applications. *J. Electrochem. Soc.* **2021**, *168*, 40504. [CrossRef]
4. Nawaz, M.; Ahmed, J.; Abbas, G. Energy-efficient battery management system for healthcare devices. *J. Energy Storage* **2022**, *51*, 104358. [CrossRef]
5. McNulty, D.; Hennessy, A.; Li, M.; Armstrong, E.; Ryan, K.M. A review of Li-ion batteries for autonomous mobile robots: Perspectives and outlook for the future. *J. Power Sources* **2022**, *545*, 231943. [CrossRef]
6. Warner, J. *Lithium-Ion Battery Chemistries: A Primer*; Elsevier: Amsterdam, The Netherlands; Oxford, UK; Cambridge, MA, USA, 2019.
7. Pan, L. The Evolution of Lithium-Ion Batteries Because of Electric Vehicles—Large Battery. Available online: https://www.large-battery.com/blog/electric-vehicles-lithium-battery-advancements-2025/ (accessed on 3 December 2025).
8. Niu, H.; Zhang, N.; Lu, Y.; Zhang, Z.; Li, M.; Liu, J.; Song, W.; Zhao, Y.; Miao, Z. Strategies toward the development of high-energy-density lithium batteries. *J. Energy Storage* **2024**, *88*, 111666. [CrossRef]
9. Kaur, G.; Gates, B.D. Review—Surface coatings for cathodes in lithium ion batteries: From crystal structures to electrochemical performance. *J. Electrochem. Soc.* **2022**, *169*, 43504. [CrossRef]
10. Oliveira Filho, H.R.; Zanin, H.; Monteiro, R.S.; Barbosa, M.H.; Teófilo, R.F. High-nickel cathodes for lithium-ion batteries: From synthesis to electricity. *J. Energy Storage* **2024**, *82*, 110536. [CrossRef]
11. Chen, Y.-S.; Dominko, R.; Marczewski, M.; Wieczorek, W. Optimizing high-energy lithium-ion batteries: A review of single crystalline and polycrystalline nickel-rich layered cathode materials: Performance, synthesis and modification. *Appl. Phys. A* **2024**, *130*, 740. [CrossRef]
12. Li, T.; Yuan, X.-Z.; Zhang, L.; Song, D.; Shi, K.; Bock, C. Degradation mechanisms and mitigation strategies of nickel-rich NMC-based lithium-ion batteries. *Electrochem. Energy Rev.* **2020**, *3*, 43–80. [CrossRef]
13. Zhao, W.; Zou, L.; Jia, H.; Zheng, J.; Wang, D.; Song, J.; Hong, C.; Liu, R.; Xu, W.; Yang, Y.; et al. Optimized Al doping improves both interphase stability and bulk structural integrity of Ni-rich NMC cathode materials. *ACS Appl. Energy Mater.* **2020**, *3*, 3369–3377. [CrossRef]
14. Sun, H.-H.; Manthiram, A. Impact of Microcrack Generation and Surface Degradation on a nickel-rich layered $LiNi_{0.9}Co_{0.05}Mn_{0.05}O_2$ cathode for lithium-ion batteries. *Chem. Mater.* **2017**, *29*, 8486–8493. [CrossRef]

15. Lim, B.-B.; Yoon, S.-J.; Park, K.-J.; Yoon, C.S.; Kim, S.-J.; Lee, J.J.; Sun, Y.-K. Advanced concentration gradient cathode material with two-slope for high-energy and safe lithium batteries. *Adv. Funct. Mater.* **2015**, *25*, 4673–4680. [CrossRef]
16. Teichert, P.; Eshetu, G.G.; Jahnke, H.; Figgemeier, E. Degradation and aging routes of Ni-rich cathode based Li-ion batteries. *Batteries* **2020**, *6*, 8. [CrossRef]
17. Pollen, H.N.; Tolchard, J.R.; Svensson, A.M.; Wagner, N.P. A single-pot co-precipitation synthesis route for Ni-rich layered oxide materials with high cycling stability. *ChemElectroChem* **2022**, *9*, e202200859. [CrossRef]
18. Díaz-Sánchez, J.; Ellingsen, I.S.; Salagre, E.; Sánchez-Prieto, J.; Maldonado, N.; Galindo, A.; Morant, C.; Vasco, E.; Garcia, G.; Rettenwander, D.; et al. Charge compensation mechanisms in Ni-rich nmc cathodes. *Batter. Supercaps* **2025**, *8*, e202500167. [CrossRef]
19. Nayak, P.K.; Grinblat, J.; Levi, M.; Wu, Y.; Powell, B.; Aurbach, D. TEM and Raman spectroscopy evidence of layered to spinel phase transformation in layered $LiNi_{1/3}Mn_{1/3}Co_{1/3}O_2$ upon cycling to higher voltages. *J. Electroanal. Chem.* **2014**, *733*, 6–19. [CrossRef]
20. Choi, J.; Dong, L.; Yu, C.-Y.; O'Meara, C.; Lee, E.; Kim, J.-H. Relationship of chemical composition and moisture sensitivity in $LiNi_xMn_yCo_{1-x-y}O_2$ for lithium-ion batteries. *J. Electrochem. Energy Convers. Storage* **2021**, *18*, 041009. [CrossRef]
21. Darjazi, H.; Rezvani, S.J.; Brutti, S.; Nobili, F. Improvement of structural and electrochemical properties of NMC layered cathode material by combined doping and coating. *Electrochim. Acta* **2022**, *404*, 139577. [CrossRef]
22. Nisar, U.; Petla, R.; Jassim Al-Hail, S.A.; Quddus, A.A.; Monawwar, H.; Shakoor, A.; Essehli, R.; Amin, R. Impact of surface coating on electrochemical and thermal behaviors of a Li-rich $Li_{1.2}Ni_{0.16}Mn_{0.56}Co_{0.08}O_2$ cathode. *RSC Adv.* **2020**, *10*, 15274–15281. [CrossRef]
23. Darjazi, H.; Gonzalo, E.; Acebedo, B.; Cid, R.; Zarrabeitia, M.; Bonilla, F.; Muñoz-Márquez, M.; Nobili, F. Improving high-voltage cycling performance of nickel-rich NMC layered oxide cathodes for rechargeable lithium–ion batteries by Mg and Zr co-doping. *Mater. Today Sustain.* **2022**, *20*, 100236. [CrossRef]
24. Tubtimkuna, S.; Danilov, D.L.; Sawangphruk, M.; Notten, P.H.L. Review of the scalable core-shell synthesis methods: The improvements of Li-Ion battery electrochemistry and cycling stability. *Small Methods* **2023**, *7*, e2300345. [CrossRef]
25. Xia, Y.; Chen, A.; Wang, K.; Xiao, Z.; Mao, Q.; Lu, X.; Wang, G.; Lu, C.; Zhang, J.; Huang, H.; et al. Binary-compositional core-shell structure Ni-rich cathode material with radially oriented primary particles in shell for long cycling lifespan lithium-ion batteries. *Mater. Today Energy.* **2023**, *34*, 101292. [CrossRef]
26. Sun, Y.-K.; Myung, S.-T.; Kim, M.-H.; Prakash, J.; Amine, K. Synthesis and characterization of $Li[(Ni_{0.8}Co_{0.1}Mn_{0.1})_{0.8}(Ni_{0.5}Mn_{0.5})_{0.2}]O_2$ with the microscale core−shell structure as the positive electrode material for lithium batteries. *J. Am. Chem. Soc.* **2005**, *127*, 13411–13418. [CrossRef]
27. García-Alonso, J.; Krüger, S.; Kelm, K.; Guney, E.; Yuca, N.; Villar-García, I.J.; Saruhan, B.; Pérez-Dieste, V.; Maestre, D.; Méndez, B. Synthesis and characterization of core–shell NMC microparticles as cathode materials for Li-ion batteries: Insights from ex situ and in situ microscopy and spectroscopy techniques. *Mater. Adv.* **2025**, *6*, 298–310. [CrossRef]
28. García-Alonso, J.; Krüger, S.; Saruhan, B.; Maestre, D.; Méndez, B. Synthesis and characterisation of core–shell microparticles formed by Ni-Mn-Co xxides. *Molecules* **2024**, *29*, 2927. [CrossRef] [PubMed]
29. Zhang, N.; Zaker, N.; Li, H.; Liu, A.; Inglis, J.; Jing, L.; Li, J.; Li, Y.; Botton, G.A.; Dahn, J.R. Cobalt-free nickel-rich positive electrode materials with a core–shell structure. *Chem. Mater.* **2019**, *31*, 10150–10160. [CrossRef]
30. Liu, Y.; Ouyang, D.; Rathore, D.; Wu, H.; Li, K.; Wang, Y.; Sha, J.; Yin, S.; Dahn, J.R. An evaluation of a systematic series of cobalt-free Ni-rich core-shell materials as positive electrode materials for Li-ion batteries. *J. Electrochem. Soc.* **2021**, *168*, 90555. [CrossRef]
31. Liu, Y.; Wu, H.; Wang, Y.; Li, K.; Yin, S.; Dahn, J.R. Impact of shell composition, thickness and heating temperature on the performance of nickel-rich cobalt-free core-shell materials. *J. Electrochem. Soc.* **2020**, *167*, 160556. [CrossRef]
32. Sun, Y.-K.; Chen, Z.; Noh, H.-J.; Lee, D.-J.; Jung, H.-G.; Ren, Y.; Wang, S.; Yoon, C.S.; Myung, S.-T.; Amine, K. Nanostructured high-energy cathode materials for advanced lithium batteries. *Nat. Mater.* **2012**, *11*, 942–947. [CrossRef]
33. Kim, U.-H.; Jun, D.-W.; Park, K.-J.; Zhang, Q.; Kaghazchi, P.; Aurbach, D.; Major, D.T.; Goobes, G.; Dixit, M.; Leifer, N.; et al. Pushing the limit of layered transition metal oxide cathodes for high-energy density rechargeable Li ion batteries. *Energy Environ. Sci.* **2018**, *11*, 1271–1279. [CrossRef]
34. Ryu, H.-H.; Park, K.-J.; Yoon, D.R.; Aishova, A.; Yoon, C.S.; Sun, Y.-K. $LiNi_{0.9}Co_{0.09}W_{0.01}O_2$: A new type of layered oxide cathode with high cycling stability. *Adv. Energy Mater.* **2019**, *9*, 1902698. [CrossRef]
35. Rathore, D.; Geng, C.; Zaker, N.; Hamam, I.; Liu, Y.; Xiao, P.; Botton, G.A.; Dahn, J.; Yang, C. Tungsten infused grain boundaries enabling universal performance enhancement of Co-free Ni-rich cathode materials. *J. Electrochem. Soc.* **2021**, *168*, 120514. [CrossRef]
36. Rathore, D.; Garayt, M.; Liu, Y.; Geng, C.; Johnson, M.; Dahn, J.R.; Yang, C. Preventing interdiffusion during synthesis of Ni-rich core–shell cathode materials. *ACS Energy Lett.* **2022**, *7*, 2189–2195. [CrossRef]

37. Becker, D.; Börner, M.; Nölle, R.; Diehl, M.; Klein, S.; Rodehorst, U.; Schmuch, R.; Winter, M.; Placke, T. Surface modification of Ni-rich $LiNi_{0.8}Co_{0.1}Mn_{0.1}O_2$ cathode material by tungsten oxide coating for improved electrochemical performance in lithium-ion batteries. *ACS Appl. Mater. Interfaces* **2019**, *11*, 18404–18414. [CrossRef] [PubMed]
38. Cai, W.; Chen, R.; Yang, Y.; Yi, M.; Xiang, L. Removal of SO_4^{2-} from Li_2CO_3 by recrystallization in Na_2CO_3 solution. *Crystals* **2018**, *8*, 19. [CrossRef]
39. Morales, J.; Pérez-Vicente, C.; Tirado, J.L. Cation distribution and chemical deintercalation of $Li_{1-x}Ni_{1+x}O_2$. *Mater. Res. Bull.* **1990**, *25*, 623–630. [CrossRef]
40. Nam, K.-W.; Bak, S.-M.; Hu, E.; Yu, X.; Zhou, Y.; Wang, X.; Wu, L.; Zhu, Y.; Chung, K.-Y.; Yang, X.-Q. Combining in situ synchrotron X-ray diffraction and absorption techniques with transmission electron microscopy to study the origin of thermal instability in overcharged cathode materials for lithium-ion batteries. *Adv. Funct. Mater.* **2013**, *23*, 1047–1063. [CrossRef]
41. Zheng, J.; Liu, T.; Hu, Z.; Wei, Y.; Song, X.; Ren, Y.; Wang, W.; Rao, M.; Lin, Y.; Chen, Z.; et al. Tuning of thermal stability in layered $Li(Ni_xMn_yCo_z)O_2$. *J. Am. Chem. Soc.* **2016**, *138*, 13326–13334. [CrossRef]
42. Rougier, A.; Gravereau, P.; Delmas, C. Optimization of the composition of the $Li_{1-z}Ni_{1+z}O_2$ electrode materials: Structural, magnetic, and electrochemical studies. *J. Electrochem. Soc.* **1996**, *143*, 1168–1175. [CrossRef]
43. Tolouei, A.; Kaflou, A.; Sadrnezaad, S.K. Effects of lithium excess and Ni content on the electrochemical performance of $Li_{1+x}(Ni_{0.45-x}Mn_{0.4}Co_{0.15})O_2$ lithium-ion cathode materials in stoichiometric state. *Mater. Res. Express* **2019**, *6*, 85522. [CrossRef]
44. Zhu, Z.; Zhu, L. Synthesis of layered cathode material $0.5Li_2MnO_3 \cdot 0.5LiMn_{1/3}Ni_{1/3}Co_{1/3}O_2$ by an improved co-precipitation method for lithium-ion battery. *J. Power Sources* **2014**, *256*, 178–182. [CrossRef]
45. Kim, U.-H.; Park, N.-Y.; Park, G.-T.; Kim, H.; Yoon, C.S.; Sun, Y.-K. High-energy W-doped $Li[Ni_{0.95}Co_{0.04}Al_{0.01}]O_2$ cathodes for next-generation electric vehicles. *Energy Storage Mater.* **2020**, *33*, 399–407. [CrossRef]
46. Kim, J. Synthesis and electrochemical behavior of $Li[Li_{0.1}Ni_{0.35-x/2}Co_xMn_{0.55-x/2}]O_2$ cathode materials. *Solid State Ion.* **2003**, *164*, 43–49. [CrossRef]
47. He, Y.; Li, Y.; Liu, Y.; Yao, N.; Li, J.; Liu, Y. Enhancement of the high-voltage electrochemical performance of an $LiNi_{0.5}Co_{0.2}Mn_{0.3}O_2$ cathode via WO_3 coating. *Appl. Surf. Sci.* **2020**, *508*, 145259. [CrossRef]
48. Heidbüchel, M.; Gomez-Martin, A.; Frankenstein, L.; Makvandi, A.; Peterlechner, M.; Wilde, G.; Winter, M.; Kasnatscheew, J. Ultrahigh Ni-rich (90%) layered oxide-based cathode active materials: The advantages of tungsten (W) incorporation in the precursor cathode active material. *Small Sci.* **2024**, *4*, 2400135. [CrossRef] [PubMed]
49. Xu, L.; Bao, C.; Zhou, H.; Li, J. The modification of WO_3 for lithium batteries with nickel-rich ternary cathode materials. *Processes* **2023**, *11*, 1756. [CrossRef]
50. Yao, X.; Xu, Z.; Yao, Z.; Cheng, W.; Gao, H.; Zhao, Q.; Li, J.; Zhou, A. Oxalate co-precipitation synthesis of $LiNi_{0.6}Co_{0.2}Mn_{0.2}O_2$ for low-cost and high-energy lithium-ion batteries. *Mater. Today Commun.* **2019**, *19*, 262–270. [CrossRef]
51. Luo, B.; Jiang, B.; Peng, P.; Huang, J.; Chen, J.; Li, M.; Chu, L.; Li, Y. Improving the electrochemical performance of $LiNi_{1/3}Co_{1/3}Mn_{1/3}O_2$ cathode material via tungsten modification. *Electrochim. Acta* **2019**, *297*, 398–405. [CrossRef]
52. Cai, J.; Yang, Z.; Zhou, X.; Wang, B.; Suzana, A.; Bai, J.; Liao, C.; Liu, Y.; Chen, Y.; Song, S.; et al. Unveiling the parasitic-reaction-driven surface reconstruction in Ni-rich cathode and the electrochemical role of Li_2CO_3. *J. Energy Chem.* **2023**, *85*, 126–136. [CrossRef]
53. Andreu, N.; Flahaut, D.; Dedryvère, R.; Minvielle, M.; Martinez, H.; Gonbeau, D. XPS investigation of surface reactivity of electrode materials: Effect of the transition metal. *ACS Appl. Mater. Interfaces* **2015**, *7*, 6629–6636. [CrossRef]
54. Fu, Z.; Hu, J.; Hu, W.; Yang, S.; Luo, Y. Quantitative analysis of Ni^{2+}/Ni^{3+} in $Li[Ni_xMn_yCo_z]O_2$ cathode materials: Non-linear least-squares fitting of XPS spectra. *Appl. Surf. Sci.* **2018**, *441*, 1048–1056. [CrossRef]
55. Dutta, A.; Homlamai, K.; Johnson, M.B.; Sawangphruk, M.; Dahn, J.R. Designing surface coating strategies with tungsten on single crystal NMC materials by XPS. *Adv. Energy Mater.* **2025**, *15*, e03051. [CrossRef]
56. Ren, H.; Wang, J.; Su, Y.; Zhao, S.; Li, C.; Wang, X.; Li, B. WO_3 coating improves the cyclic stability of $LiNi_{0.9}Co_{0.05}Mn_{0.05}$ as cathode materials for lithium-ion batteries. *Electrochim. Acta* **2024**, *503*, 144913. [CrossRef]
57. Malik, M.; Chan, K.H.; Azimi, G. Review on the synthesis of $LiNi_xMn_yCo_{1-x-y}O_2$ (NMC) cathodes for lithium-ion batteries. *Mater. Today Energy* **2022**, *28*, 101066. [CrossRef]
58. Nisar, U.; Muralidharan, N.; Essehli, R.; Amin, R.; Belharouak, I. Valuation of surface coatings in high-energy density lithium-ion battery cathode materials. *Energy Storage Mater.* **2021**, *38*, 309–328. [CrossRef]
59. Chu, G.; She, Y.; Huang, A.; Ye, Q.; Deng, Y.; Lin, T.; Sun, Y.; Schülli, T.U.; Wang, L.; Zhu, X. Volmer-Weber growth of nano-island heterostructures on spinel cathodes: A route to stable high-voltage lithium-ion batteries. *Chem. Sci.* **2025**, *16*, 23282–23291. [CrossRef]
60. Zhao, C.; Yin, X.; Huang, Y.; Zhang, X.; Jiang, W.; Zhou, Z.; Tu, W.; Wang, X.; Wang, D.; Duan, J. Facile modification using organic acid molecules to neutralize residual alkaline compounds for stabilizing $LiNi_{0.95}Co_{0.04}Mn_{0.01}O_2$ cathode material. *Energy Mater. Devices* **2025**, *3*, 9370056. [CrossRef]

61. Li, W.; Lee, S.; Manthiram, A. High-nickel NMA: A cobalt-free alternative to NMC and NCA cathodes for lithium-ion batteries. *Adv. Mater.* **2020**, *32*, e2002718. [CrossRef]
62. Middlemiss, L.A.; Rennie, A.J.; Sayers, R.; West, A.R. Characterisation of batteries by electrochemical impedance spectroscopy. *Energy Rep.* **2020**, *6*, 232–241. [CrossRef]
63. Meddings, N.; Heinrich, M.; Overney, F.; Lee, J.-S.; Ruiz, V.; Napolitano, E.; Seitz, S.; Hinds, G.; Raccichini, R.; Gaberšček, M.; et al. Application of electrochemical impedance spectroscopy to commercial Li-ion cells: A review. *J. Power Sources* **2020**, *480*, 228742. [CrossRef]
64. Schmitz, R.W.; Murmann, P.; Schmitz, R.; Müller, R.; Krämer, L.; Kasnatscheew, J.; Isken, P.; Niehoff, P.; Nowak, S.; Röschenthaler, G.-V.; et al. Investigations on novel electrolytes, solvents and SEI additives for use in lithium-ion batteries: Systematic electrochemical characterization and detailed analysis by spectroscopic methods. *Prog. Solid State Chem.* **2014**, *42*, 65–84. [CrossRef]